Article

# Study of Mid-Pressure Ar Radiofrequency Plasma Used in Plasma-Enhanced Atomic Layer Deposition of α-$Al_2O_3$

Carl-Thomas Piller , Jüri Raud * , Lauri Aarik , Indrek Jõgi , Rasmus Talviste , Jaan Aarik

Posted Date: 4 March 2024

doi: 10.20944/preprints202403.0133.v1

Keywords: capacitively coupled plasma, argon plasma, plasma enhanced atomic layer deposition, optical emission spectroscopy

doi:10.20944/preprints202403.0133.v1

*Article*

# Study of Mid-Pressure Ar Radiofrequency Plasma Used in Plasma-Enhanced Atomic Layer Deposition of $\alpha$-$Al_2O_3$

**Carl-Thomas Piller, Jüri Raud *, Lauri Aarik, Indrek Jõgi, Rasmus Talviste and Jaan Aarik**

University of Tartu, Institute of Physics, W. Ostwaldi str. 1, 50411, Tartu, Estonia
* Correspondence: juri.raud@ut.ee

**Abstract:** This study investigated the characteristics of radio-frequency middle-pressure argon plasma used in the atomic layer deposition (ALD) of $Al_2O_3$ films. Based on the electrical characteristics, that is current, voltage, and phase shift between them, and stability of plasma plume, the optimum plasma power, allowing reliable switching on the plasma for any step of an ALD cycle, was determined. Spectral measurements were performed to determine the gas temperature and reactive species that could be important in the ALD process. The density of metastable argon atoms was estimated using tunable laser absorption spectroscopy. It was concluded that plasma heating of substrates did not affect film growth and proposed that the crystallization-enhancing effect of plasma was due to the action of OH radicals, produced in the plasma.

**Keywords:** capacitively coupled plasma; argon plasma; plasma enhanced atomic layer deposition; optical emission spectroscopy

## 1. Introduction

Extensive research has been conducted on aluminum oxide as a thin-film material with diverse applications including protective coatings, diffusion barriers, and electronic and optical devices. Crystalline $Al_2O_3$ films offer clear advantages in applications that require elevated chemical stability, specific optical or electronic attributes, and superior mechanical properties. The deposition of crystalline $Al_2O_3$ thin films using traditional thermal atomic layer deposition (ALD) is challenging. The use of plasma during the ALD process (PEALD) has the potential to facilitate the process as it can reduce energy consumption and enable growth of crystalline thin films with higher density at a reduced growth temperature (TG) compared to the thermal ALD processes [1]. The main functions of plasma in the ALD process are

(i) generation of reactive species that participate in surface reactions [2–7], and
(ii) energy delivery to treated surface.

Reactive plasma species such as metastable state atoms and molecules and vibrationally excited molecules can promote film growth by delivering their potential energy to the film via Auger processes [8], thereby reducing the activation energy of the reactions [2]. When the ALD process occurs in the active plasma region, energy transfer to the film surface can also occur via ions and heavy particles impacting the surface with high kinetic energy. In this case, the temperature of the impact site increases locally because of the momentum exchange between these particles and film lattice atoms, enabling crystalline film growth at lower substrate temperatures [1]. Plasmas offer the flexibility to produce specific reactive species, for example, by choosing a suitable gas composition and gas pressure, and tailoring gas-phase chemistry with ALD surface reactions to obtain thin films with specific properties [9].

Capacitively coupled plasma is a commonly used plasma source in PEALD reactors, which based on geometry, can be divided into direct and indirect treatment devices [1]. In the case of the direct treatment, the substrate is placed directly into the plasma on an electrode; therefore, the deposited films experience reactions of neutral plasma species diffused to the film as well as the impact of ions. Indirect-treatment devices utilize remote plasma sources, and substrates are placed in the plasma particle effluent, which mostly consists of long-lifetime reactive species. The production of reactive species (e.g., O, $O_3$, H, OH, N, $N_2$(A), $NH_x$) occurs in the plasma of molecular gas or inert gas with a molecular gas admixture [9–12], whereas higher concentrations of molecular gas have been found to be favorable with respect to the reactive species yield [13]. At the same time, the increase in the molecular content impedes discharge ignition, which forces to increase the voltage needed for the discharge ignition and sustaining [14], which in turn could increase the plasma switching time jitter and force the plasma to run in the high-current, $\gamma$-mode. The high-current mode has been found to worsen the film uniformity compared to that produced using a low-current $\alpha$-mode [15]. A possible solution for lowering the plasma ignition voltage while still producing reactive species is to use remote inert gas plasma that is mixed with molecular gases downstream from the plasma source. Such an arrangement has rarely been studied, although it has been found to provide a more stable discharge and even increase in the yield of reactive species [16].

In our previous study [17], we investigated the influence of Ar plasma applied during different steps of the ALD process on the growth of $Al_2O_3$ from the trimethylaluminum (TMA) and water ($H_2O$) vapor. The Ar plasma was mixed with the precursors downstream of the plasma source. According to the X-ray reflection (XRR) studies of the films deposited at substrate temperature of $T_G$ = 650 K on Si(100), the application of plasma during the $H_2O$ pulse and during the purge periods following the TMA and $H_2O$ pulses caused an increase in the densities of the films compared with the densities of the films deposited by thermal ALD, that is, without plasma excitation. However, all films obtained on bare Si(100) substrates were amorphous, and the increase in density caused by plasma excitation did not exceed 2%. More remarkable changes were caused by plasma excitation to the properties of the $Al_2O_3$ thin films deposited on the $\alpha$-$Cr_2O_3$ seed layers. According to the X-ray diffraction (GIXRD) studies, the films deposited at $T_G \geq 600$ K on $\alpha$-$Cr_2O_3$ seed layers using the Ar plasma during the purge after the $H_2O$ pulse contained the $\alpha$-$Al_2O_3$ phase, whereas the films deposited using thermal ALD were amorphous.

As the growth of $\alpha$-$Al_2O_3$ at these relatively low $T_G$ values is of marked importance for many applications, a more extensive study of plasma processes causing this effect was performed in the research described in this paper. Electrical measurements, spatiotemporal optical emission spectroscopy and tunable diode laser absorption spectroscopy (TDLAS) were used to determine the plasma parameters that could influence the PEALD process.

## 2. Materials and Methods

The experimental setup (Figure 1) has been described in our previous study [18]. Here, the more specific details are focused on. The plasma was ignited using a 13.6 MHz RF generator coupled with a BDS-AMN 750 automatic matching network (both produced by BDISCOM SRL).

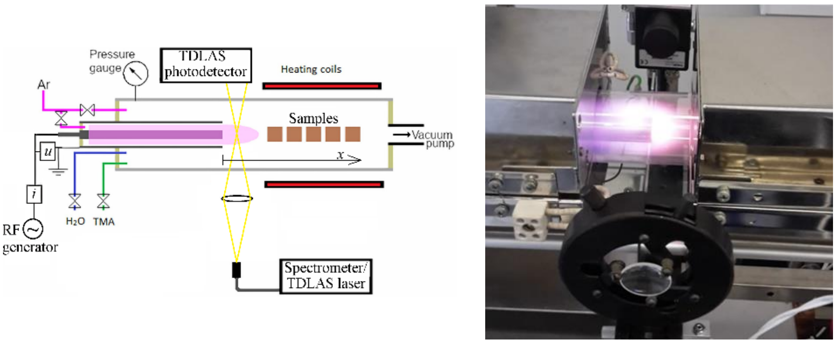

(**a**) (**b**)

**Figure 1.** (**a**) Schematic representation of the experimental device; (**b**) Photo of PEALD.

The generator output power, fixed at 30 W, was switched on and off by using a signal from the ALD process controller. At this generator power, the output voltage was sufficiently high for instant ignition of the plasma. A coaxial electrode configuration was used. The diameter of powered central stainless-steel electrode was 6.4 mm and the inner diameter of grounded surrounding stainless-steel tube was 16 mm (hereafter- “plasma tube”). The length of each electrode was 500 mm. The diameter of the quartz tube isolating the reactor from ambient air was 47 mm. The overall flow of Ar through the reactor was 300 sccm, whereas the flow through the plasma tube was 150 sccm. The pressure in the reactor was 1.9-2.1 Torr. TMA (98%) and $H_2O$ were used as precursors in the ALD film deposition, and carried by a 300 sccm Ar (99.999%) flow,. The durations of the TMA and $H_2O$ pulses and the TMA purge were 2 s, while that of the $H_2O$ purge was 5 s. $Al_2O_3$ films were deposited on a Si(100) substrate covered with an $\alpha$-$Cr_2O_3$ seed layer. The deposition of the seed layer is described in a previous study [18]. The samples were inserted into the reaction chamber on a $SiO_2$ holder. The temperature of the samples was recorded prior to the ALD cycles after the temperature stabilization using a K-type thermocouple.

The phase composition, thickness, density, and roughness of the films was measured using a SmartLab (Rigaku) diffractometer and analyzed using the GIXRD and XRR methods. The optical emission spectra of the plasma were recorded along the plasma axis at different distances ($x$) from the plasma tube orifice (Figure 1a) using Ocean Insight HR4 PRO (spectral range 274–414 nm, resolution around 0.1 nm) and Ocean Optics USB4000 (spectral range 185–850 nm, resolution around 1 nm) spectrometers. Because of the moderate spectral resolution of the USB4000 spectrometer, some spectral lines were not resolved and were deconvoluted using a nonoverlapped Ar spectral line at 696.5 nm as an instrumental function. An example of the deconvoluted lines is shown in Figure 2.

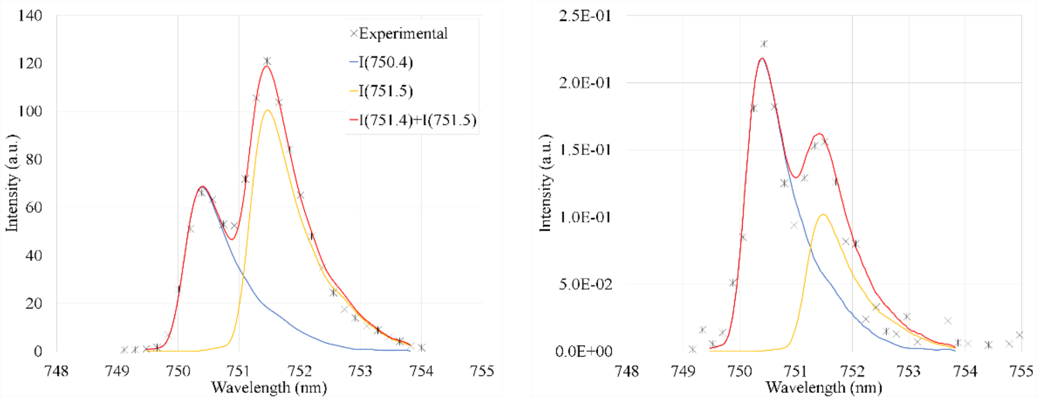

(**a**) (**b**)

**Figure 2.** Example of experimental and deconvoluted Ar spectral lines at 750.4 and 751.5 nm (**a**) in Ar discharge and (**b**) during TMA pulse (2 s after opening TMA valve).

The fitting of the experimental and calculated spectra used for the estimation of rotational temperature and the concentration of Ar atoms in the metastable state $1s_5$ (Paschen notation) was performed using the MathCad software function *Minimize*. Electrical characteristics were recorded using the oscilloscope Tektronix TDS-540B. The voltage ($u$) was measured using a 1:100 Tektronix voltage probe P5100, while the current ($i$) was measured using a McPherson current monitor 6585. The concentration of Ar $1s_5$ state atoms was estimated using a TDLAS unit. The scan range of the Littman-type external cavity diode laser Thorlabs TLK-L780M with a power of 50 mW was 740–800 nm and the line width was < 130 kHz. The free spectral range and finesse of Fabry–Perot interferometer Thorlabs SA-200, used to check the laser operation stability and to calibrate the relative wavelength, were 1.5 GHz and 200 respectively. A photodetector Thorlabs APD110A2 coupled with an interference filter with a central wavelength of 763.5 nm and a full width at half maximum of 40 nm was used to register the laser signal.

doi:10.20944/preprints202403.0133.v1

## 3. Results and Discussion

### 3.1. Plasma Characteristics

#### 3.1.1. Discharge Appearance and the Choice of Generator Power

The appearance of the discharge depended on the generator power. At low power values, the radiation intensity in the plasma tube was low, and the space between the electrodes was only partly filled with plasma. An increase in the generator power caused the gradual filling of the tube with plasma, and finally, the emergence of a plasma plume outside the tube. At a generator power of 30 W and after a long-term Ar purge, the bright plasma plume of Ar discharge extended outside the tube to a distance of 2–3 cm, while the diameter of the plume was somewhat larger than that of the outer electrode, as shown in Figure 1b. A very low-intensity plasma column was observed at longer distances (up to 10 cm). By further increasing the generator power, randomly located irregular plasma sparks in addition to the homogenous plasma appeared between the electrodes. With the appearance of sparks, instabilities in the plasma plume outside the tube were observed. Therefore, ALD was conducted at a generator power of 30 W. Outside the tube, the discharge appearance also depended on the ALD step. The TMA and $H_2O$ pulses caused a rapid reduction in the extent of the plasma plume outside the plasma tube and changed the plasma color. During the following purge, plasma extension was gradually restored.

#### 3.1.2. Electrical Characteristics

Plasma power was calculated from the current and voltage waveforms as described in our previous studies [19,20]. When the plasma was produced at a low generator power, the waveforms exhibited a sinusoidal shape, similar to that observed without discharge. At a generator power of 30 W, the current waveform deviated significantly from a sinusoidal waveform, as shown in Figure 4. The irregular shape of the current waveform can be explained by the different areas of powered and grounded electrodes.

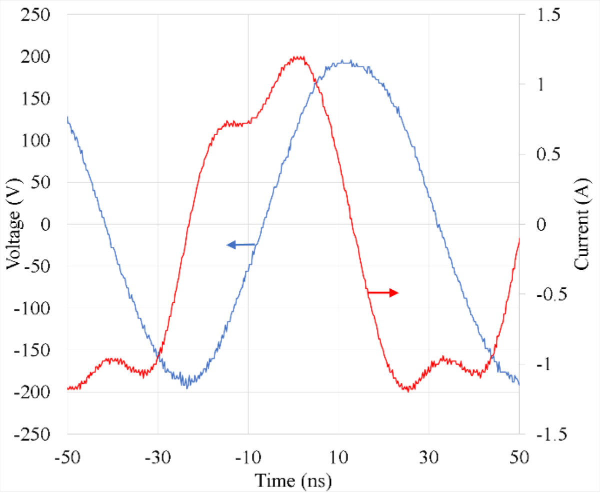

**Figure 4.** An example of measured current and voltage waveforms. The phase shift component due to different lengths of connecting cables and parasitic capacitance was considered in the graph.

The plasma power was estimated using the formula $P = \frac{1}{T}\int_0^T i_\mathrm{p}(t)\, u_\mathrm{p}(t)\mathrm{d}t$. The phase shift component caused by different lengths of the connecting cables, parasitic capacitance, etc., was determined from the measured $u$ and $i$ waveforms without discharge, and it was considered in the plasma power calculation. At a generator power of 30 W, the phase shift between $i$ and $u$ was 84.2 ± 1.0°, and the plasma power was 11.6 ± 1.8 W. The plasma power did not depend on the Ar plasma gas flow rate in the plasma tube (tested in the range of 100–300 sccm) or on the gas composition outside the plasma tube in the reactor. Hence, the plasma power was completely determined by the Ar discharge inside the plasma tube.

### 3.1.3. Plasma spectrum

The optical emission spectra recorded at a distances 5 and 50 mm is shown in Figure 5a,b. In the case of the Ar plasma, the most intense spectral lines belonged to Ar. Because of impurity additives in Ar (due to leakage, etc.), a weak atomic oxygen line at 777 nm and bands of OH at 308 nm, the $N_2$ first positive system (FPS) at 550–700 nm, and a second positive system (SPS) at 300–400 nm were observed. The deconvolution of the $N_2$(C-B,0-0) band also revealed the presence of an NH(A-X,0-0) band at 336 nm (Figure S1). The start of the TMA pulse caused a rapid decrease in the intensity of the aforementioned molecular bands and atomic lines (Figures 5c, time interval $\Delta t$ = 10–15 s). As a result of TMA ($Al_2(CH_3)_6$) decomposition, bright Al lines at 308.22, 309.27, 394.40 and 396.15 nm appeared in the spectra. During the following purge ($\Delta t$ = 15–25 s), the intensity of the Ar lines and $N_2$ bands gradually increased and became even more intense than before the ALD pulses, whereas the OH intensity decreased due to $H_2O$ removal in reaction with TMA. The emission of CN radicals at 358, 388, and 416 nm, CH at 386 and 431 nm, and $C_2$ at 516.2 nm were identified from the molecular bands [21–24]. Interestingly, although the appearance of these bands is also related to TMA decay, they were not observed during the TMA pulse but during the TMA purge. A possible reason for this observation is the increase in the electron temperature and density during TMA purge, which enabled the production and excitation of these molecules. Similar to the TMA pulse, the $H_2O$ pulse ($\Delta t$ = 25–30 s) reduced the intensities of all spectral lines and $N_2$ bands with the exception of the OH band. The increased production of OH excited states molecules can be attributed primarily to the reaction between Ar $1s_{2\ldots5}$ atoms and $H_2O$ molecules [25–27]. During the purge following the $H_2O$ pulse ($\Delta t$ = 30–40 s), the intensities of the Ar lines and $N_2$ bands gradually increased, whereas the OH intensity reached a sharp maximum at ~ 1 s after the end of the $H_2O$ pulse and then started to decrease.

With an increase in the distance $x$ the intensities of all bands and lines decreased; however, the general trends remained similar, as described above (Figure 5b,d).

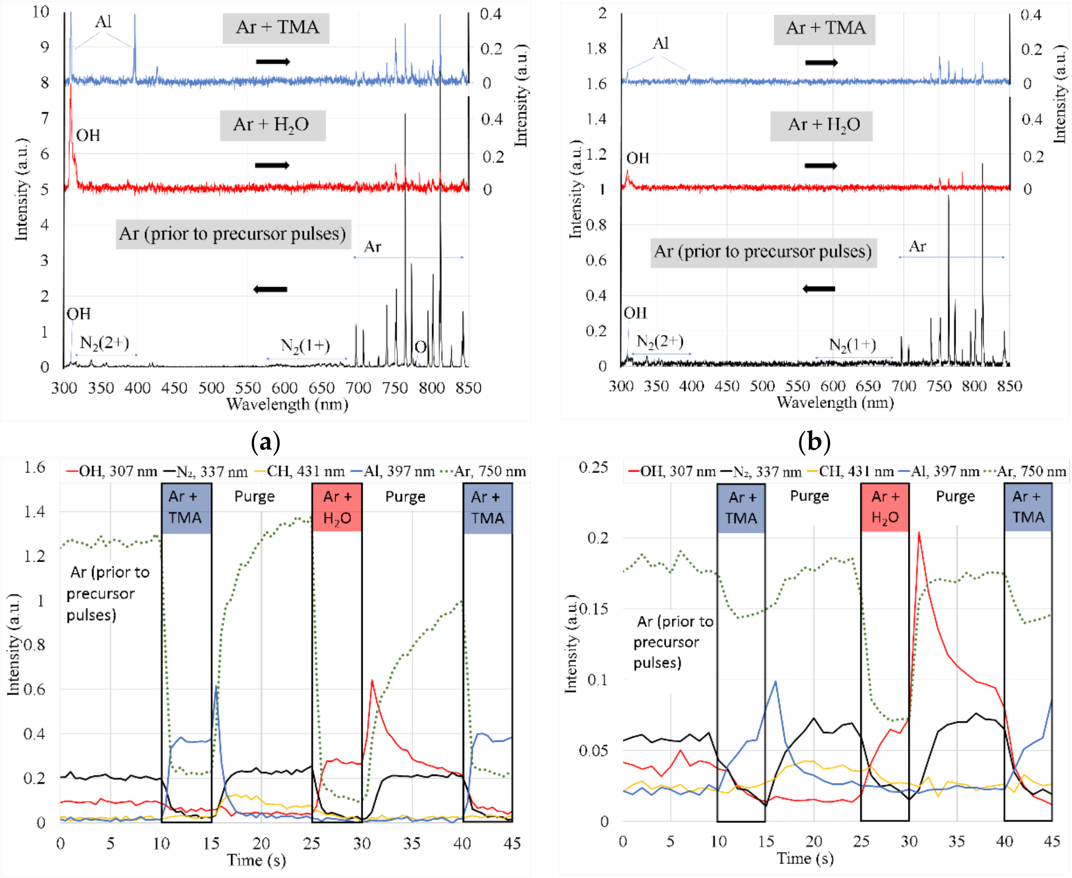

(a)

(b)

(**c**) (**d**)

**Figure 5.** (**a**,**b**) Spectra of Ar plasma after long-term Ar purge, and during $H_2O$ (Ar+$H_2O$) or TMA (Ar+TMA) pulses recorded at (**a**) $x$ = 5 mm and (**b**) $x$ = 50 mm. The spectra during $H_2O$ and TMA pulses were recorded 2 s after opening the corresponding valve. The intensity scale of the corresponding spectrum is indicated by the black arrow; (**c**,**d**) Intensities of OH (307 nm), $N_2$ (337 nm), CH (431 nm) bandheads, and Al (397 nm) and Ar (750 nm) lines recorded prior to ALD pulses (0–10 s) and during the TMA pulse (10–15 s), the first purge (15–25 s), $H_2O$ pulse (25–30 s), the second purge (30–40 s), and TMA pulse (40–45 s) at (**c**) $x$ = 5 mm and (**d**) $x$ = 50 mm. Plasma was turned on for the whole measurement period (0–45 s).

### 3.1.4. Gas Temperature

The plasma gas temperature ($T_{gas}$) was estimated using different methods. Firstly, $T_{gas}$ was estimated on the basis of the $N_2$(C) rotational temperature ($T_{rot}$) calculated for several vibrational transitions, as described in our previous study [28]. In the case of electron impact excitation of $N_2$(C), $T_{rot} \approx T_{gas}$. However, in the Ar discharges, $T_{rot}$ of these molecules could be influenced by the energy transfer from the metastable Ar atoms, which can result in remarkably higher $T_{rot}$ values than $T_{gas}$ [28]. The rotational temperatures of the $N_2$ SPS vibrational transitions 0-2 (bandhead at 380 nm), 1-3 (375 nm) and 2-4 (371 nm) (Figure 6) were estimated in Ar discharge (after a long-term Ar purge) to reduce the interference of TMA/$H_2O$ additives on the rotational spectra. The temperature near the plasma tube orifice estimated under such conditions is expected to be somewhat higher than that during ALD pulses because the plasma plume extension outside the plasma tube was largest in the case of pure Ar discharge, and the plasma power was insensitive to the gas composition outside the plasma tube (Section 3.1.2).

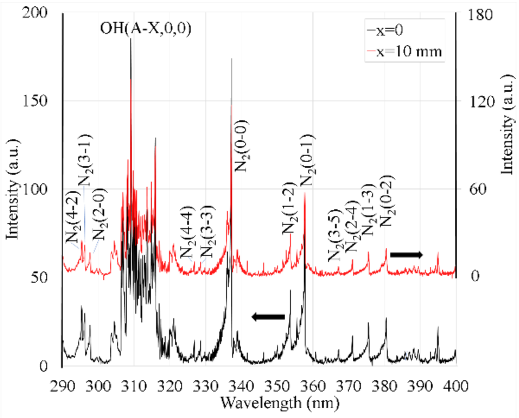

**Figure 6.** Spectra of OH(A-X,0-0) and several bands of $N_2$ SPS registered with an Ocean Insight HR4 PRO spectrometer at distances $x$ = 0 and $x$ = 10 mm. The reaction chamber heater was turned off. In brackets, $N_2$ SPS vibrational transitions are shown. The intensity scales of corresponding spectra are shown by black arrows.

Examples of the recorded and calculated spectra of the $N_2$ SPS vibrational transitions 0-2 and 2-4 are shown in Figure 7a. The lowest rotational temperature, $T_{rot} \approx 450 \pm 100$ K, among the studied $N_2$ SPS vibrational transitions was found for $N_2(C,v=2)$ near the plasma tube orifice ($x$ = 0 mm), and it diminished with distance (Figure 7b). At $x > 10$ mm, the $N_2$(C-B,2-4) band intensity was too low for the reliable estimation of temperature.

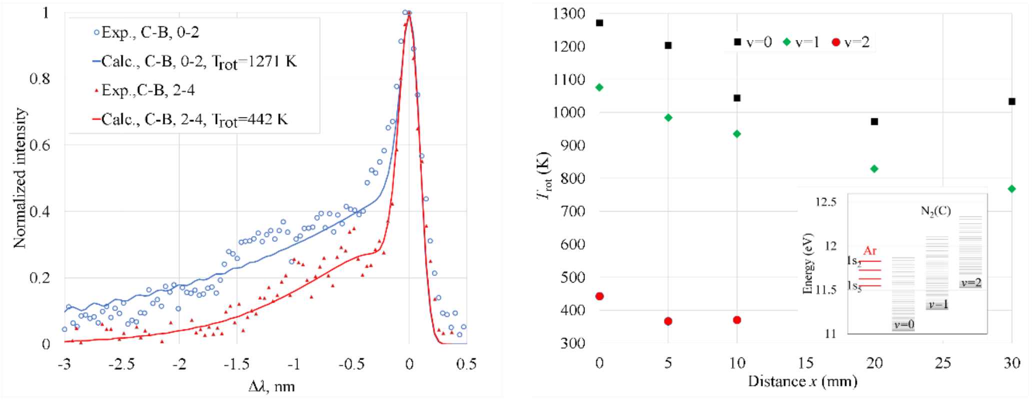

(**a**) (**b**)

**Figure 7.** (**a**) Example of registered and calculated spectra of $N_2$(C-B) 0-2 and 2-4 vibrational transitions at the distance $x$ = 0. (**b**) Rotational temperature of $N_2$(C, $v$=0,1,2) as a function of $x$. Inset depicts the energy levels of Ar metastable ($1s_3$ and $1s_5$) and resonant ($1s_2$ and $1s_4$) state atoms and $N_2$ rotational states (up to $J$=60) for vibrational states $v$=0, 1, 2.

Considerably higher $T_{rot}$ values were found for the $N_2$(C,$v$<2) vibrational states, reaching 1300 K for $N_2$(C,$v$=0) and ≈1100 K for $N_2$(C,$v$=1) (Figure 7b). This dependence of $T_{rot}$ on the number of vibrational states $v$ can be explained by the excitation transfer from the Ar metastable state atoms $\mathrm{Ar}(1\mathrm{s}_2 \ldots 1\mathrm{s}_5) + \mathrm{N}_2(\mathrm{X}) \rightarrow \mathrm{Ar} + \mathrm{N}_2(\mathrm{C})$, which can cause an overpopulation of higher rotational levels when comparing the population distribution corresponding to the equilibrium with $T_{gas}$ [28]. From an energetic point of view, the ability to populate higher rotational states via this reaction decreases for higher values of $v$, as shown in the inset of Figure 5b, and the reaction rate coefficient also decreases with the vibrational number. For example, at 300 K, the ratio of the rate coefficients for the population $v$ = 0, 1, and 2 states is 1:0.25:0.1 [29]. Therefore, with trace amounts of $N_2$ in Ar plasmas, lower vibrational levels are more susceptible to the overpopulation of higher rotational levels than higher vibrational levels. At higher pressures, the neutral particle collisions can still thermalize the rotational population distribution even for the vibrational state $N_2$(C,$v$=0) and enable $T_{rot}$ to be used as $T_{gas}$ estimate [30]; at the low pressure used in our experiment, the thermalization is apparently too slow, and $T_{rot}$ from $N_2$(C,$v$<2) overestimates $T_{gas}$.

An attempt to determine $T_{gas}$ was made using the OH(A-X,0-0) transition, which has been used to estimate $T_{gas}$ at higher pressures [31]. In our spectra, the OH(A-X,0-0) band at 307 nm is one of the brightest peaks during the $H_2O$ pulse and the following purge (Figure 6). Similar to $N_2$(C,v<2), higher rotational levels of OH(A,0) can be excited by the energy transfer from excited Ar atoms, which results in $T_{rot}$ higher than that expected from $T_{gas}$ [26]. The radiative lifetime of OH(A,$v$=0) is remarkably longer than that of the $N_2$ SPS bands [28]. Therefore, the rotational relaxation can still be expected to achieve a population distribution equilibrium with $T_{gas}$. However, in our plasma, OH(A $v$=0) $T_{rot}$ also overestimated $T_{gas}$, as the temperature determined using Lifbase software [32], $T_{rot}$($x$=0) = 1300 K, was remarkably higher than that of $N_2$(C,$v$=2). Apparently, the relaxation was still too slow at our gas pressure.

The gas temperature was additionally estimated by analyzing the absorption shape of the 763.5 nm line, which was determined using the TDLAS technique. The shape of the line depends on $T_{gas}$ [33,34]; and the temperature estimation procedure is described in Figure S2. The remarkable fluctuation of the laser emission of our TDLAS setup (Figure S3) and the low signal-to-noise ratio prevented the reliable determination of $T_{gas}$ as a function of the distance $x$. At $x$ = 0, the determined temperature was 700 ± 200 K (Figure S2). This coincided with $T_{rot}$ of $N_2$(C,$v$=2) within the uncertainty margins.

The knowledge of the plasma power also allows a rough estimation of the $T_{gas}$ [35]. Under stationary conditions $T_{gas} = T_E + \frac{w}{n_0 \cdot C_p \cdot v_H}$, where $T_E$ is the temperature of plasma tube, $w$ ≈0.14 W cm-

Preprints.org (www.preprints.org) | NOT PEER-REVIEWED | Posted: 4 March 2024 doi:10.20944/preprints202403.0133.v1

$^3$ is the power density, $n_0$ is the gas density, $C_P \approx 3.3 \cdot 10^{-23}$ J/K is the specific heat of Ar at constant pressure per atom and $\nu_H = \frac{8 \cdot \lambda_{Ar}}{n_0 \cdot c_P \cdot r^2} + \frac{2 \cdot v_{gas}}{L}$ is the heat removal frequency. Here $\lambda_{Ar}$ is the Ar thermal conductivity (0.0177 W/(K·m)), $r$ = 8 mm is the inner radius of the plasma tube, $v_{gas}$ the linear velocity of the gas (5.9 m/s) in the plasma tube, and $L$ = 500 mm is the length of the plasma tube. The first and second terms in the formula used for the calculation of $\nu_H$ give the heat removal frequency by heat conduction and convective heat transport, respectively. Under our conditions, the contribution of the heat removal by convective heat transport is ≈2.3%. Therefore, $T_{gas}$ depends only slightly on $n_0$. Presuming $T_E$ is stabilized at room temperature, the calculated $T_{gas}$ near the plasma tube orifice is $T_{gas} \approx 360$ K. Actually, $T_E$ is probably higher owing to poor cooling of the plasma tube; however, it is expected to be lower than the maximum temperature of the O-rings of our vacuum system (ERIKS' 51414 green, $T_{max}$ = 473 K). This gives the upper limit of the $T_{gas}$ of 540 K, which also coincides with the $T_{rot}$ of $N_2(C,v=2)$ within the uncertainty margins. Therefore, in the following, we used the $T_{rot}$ of $N_2(C,v=2)$ as the $T_{gas}$.

### 3.1.5. Line-Integrated Concentration of Ar Metastable, 1s$_5$ State Atoms

The concentration of metastable Ar 1s$_5$ state atoms ([Ar(1s$_5$]) was determined in the Ar discharge on the basis of Ar spectral line $\lambda_0$= 763.5106 nm absorption (transition 1s$_5$→2p$_6$) [36] using the TDLAS technique [33]. The estimation was performed x values 0–10 mm as at longer distances the absorption was below the detection limit of our TDLAS apparatus. The optical depth (OD) (Figure 8a) was determined as $\mathrm{OD} = \ln\left(\frac{I_0}{I_t}\right) = k(\lambda) \cdot l$, where $I_t$ and $I_0$ are the laser intensities with and without the plasma, respectively, $k$ and $l$ are the absorption coefficient and absorption length, respectively.

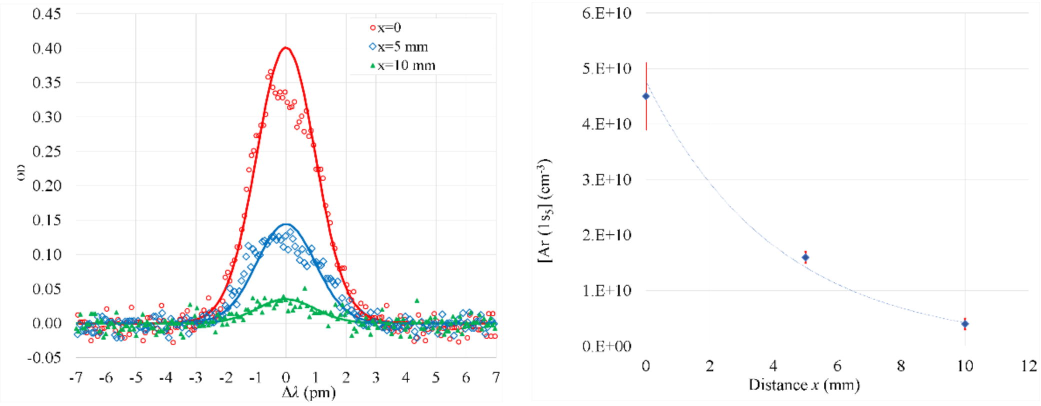

(**a**) (**b**)

**Figure 8.** (**a**) Optical depth (OD) of Ar absorption line at 763.5 nm for different $x$. The absorption line profile was fitted with Voigt function shown by solid lines; (**b**) Ar 1s$_5$ state atoms concentration, [Ar(1s$_5$)] as a function of $x$. Solid line represents the exponential trendline of datapoints. Error bars shown in the figure are found as differences of Ar(1s$_5$) concentrations calculated on the basis of experimental OD and the Voigt fitting.

The concentration of Ar(1s$_5$) state atoms was calculated using the experimentally determined OD according to the formula $[\mathrm{Ar}(1s_5)] = \frac{8 \cdot \pi \cdot g_i \cdot c}{\lambda_0^4 \cdot g_j \cdot A_{ij} \cdot l} \int k(\lambda) \cdot l \cdot d\lambda$ [33]. Here, $g_i$ = 5 and $g_j$ = 5 are the statistical weights of the upper and lower states, respectively; $c$ is the speed of light; $A_{ij} = 2.45 \cdot 10^7$ s$^{-1}$ is the Einstein coefficient; $\lambda_0$ = 763.5106 nm is the center wavelength of the absorption transition [23], and $l$ = 20 mm is the absorption length. The concentration of Ar(1s$_5$) atoms decreased with increasing $x$ almost exponentially from $4.5 \cdot 10^{10}$ to $4 \cdot 10^9$ cm$^{-3}$ when $x$ increased from 0 to 10 mm.

Introduction of any ALD precursor caused a decrease in the concentration of Ar(1s$_5$) below the detection limit of our TDLAS apparatus. However, the spectral measurements indicated that during TMA and $H_2O$ pulses Ar(1s$_{2...5}$) concentrations were very low. Compared with the other Ar spectral lines, the intensity of the Ar line at 750.4 nm was less sensitive to the introduction of TMA and $H_2O$. The rate coefficient for the population of the upper state of this transition, $2p_1$, via the direct electron impact excitation from the ground state, is higher than that for other 2p-1s transitions observed in the spectra, whereas for other transitions, the stepwise excitation from Ar $1s_{2...5}$ is more important [37]. As an example, Figure 2 shows intensities of spectral lines at 750.4 (transition $2p_1 \rightarrow 1s_2$) and 751.5 nm (transition $2p_5 \rightarrow 1s_4$) registered from Ar plasma and during a TMA pulse. The 751.4 nm line was more intense in the Ar discharge prior to the ALD pulses and also during the purge periods, but during the TMA and $H_2O$ pulse the 750.4 nm line dominated. Notably, the ratio of the rate coefficients for the direct electron impact excitation to $2p_1$ and $2p_5$ was approximately 2 [37] in the electron temperature range $T_e$ = 2.5–3.5 eV. This is close to the intensity ratio of the transitions $2p_1 \rightarrow 1s_2$ and $2p_5 \rightarrow 1s_4$ (Figure 2b). Considering similar Einstein coefficients of these transitions ($A_{750.4}=4.5\cdot10^7 s^{-1}$, $A_{751.5}=4.0\cdot10^7 s^{-1}$ [36]), this finding indicates negligible stepwise excitation of Ar states during the TMA and $H_2O$ pulse due to very efficient quenching of the $1s_{2...5}$ states.

### *3.2. Effect of Plasma on Film Properties*

The ALD process used for deposition of films for post-growth studies consisted of ALD cycles, repeated 1000 times. Each cycle contained the following steps: TMA pulse (duration 2 s), purge (2 s), $H_2O$ pulse (2 s), and purge (5 s), whereas it was possible to switch the plasma on for any step. Our previous study [17] revealed that the plasma applied during the TMA pulse caused TMA decomposition, resulting in low-density amorphous $Al_2O_3$ films. It was also found that plasma had a detrimental effect on crystal growth when applied during the TMA purge, whereas in this case, the film growth per cycle (GPC) and density were similar to those of thermal ALD. As indicated by the intensity decay of the Al spectral lines (Figure 5c), the TMA residuals were removed from the gas within 1-2 s of the TMA pulse. Similar, fast TMA removal after TMA pulse was also concluded from Q-pod quartz crystal microbalance (QCM) measurements [17]. With a decrease in the intensity of the Al lines during the TMA purge, CH, CN, and $C_2$ bands appeared in the spectrum (Figure 5c) and were observed during the entire TMA purge step. The appearance of these bands, but not Al lines, indicates that plasma applied during the TMA purge caused decomposition of surface intermediate species formed during the TMA ($Al_2(CH_3)_6$), pulse. This enables the formation of excited CH, CN, and $C_2$ molecules via plasma-chemical reactions involving desorbed $CH_x$ species. Al atoms remain on the surface, which explains why the GPC and density of the film were not affected by the plasma applied during the purge following the TMA pulse.

The plasma excitation, applied during the purge following the $H_2O$ pulse or during the $H_2O$ pulse and the following purge, most significantly contributed to the increase in the density and crystallization of the $Al_2O_3$ films grown on the $\alpha$-$Cr_2O_3$ seed layers. This effect enabled us to obtain $\alpha$-$Al_2O_3$ in the films deposited at 600 K (Figure 9).

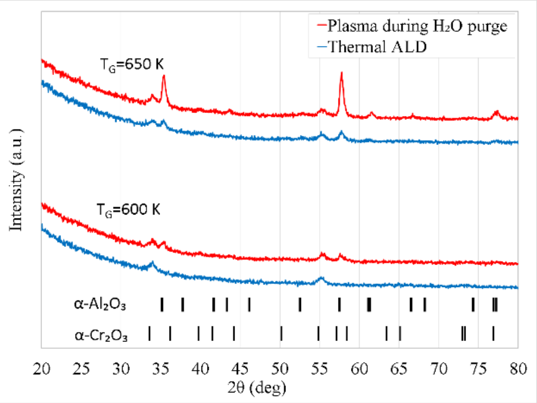

**Figure 9.** GIXRD diffractograms of $Al_2O_3$ films deposited on $\alpha$-$Cr_2O_3$ at substrate temperatures 600 and 650 K by thermal ALD and PEALD, (plasma turned on during the $H_2O$ purge). During deposition the samples were located at a distance of 20 mm from the outlet of plasma tube. Reflections peaking at 35.3 and 57.6° indicate formation of $\alpha$-$Al_2O_3$.

doi:10.20944/preprints202403.0133.v1

The film growth depended on the distance between the samples and orifice of the plasma tube. At a distance $x$ = 20 mm, the plasma applied during the purge following the $H_2O$ pulse significantly enhanced the growth of $\alpha$-$Al_2O_3$ as shown in Figure 10. By contrast, the GIXRD diffractograms of films deposited by PEALD and thermal ALD at $x$ = 70 mm were similar. Consequently, the plasma influence on the crystal growth was negligible in the latter case.

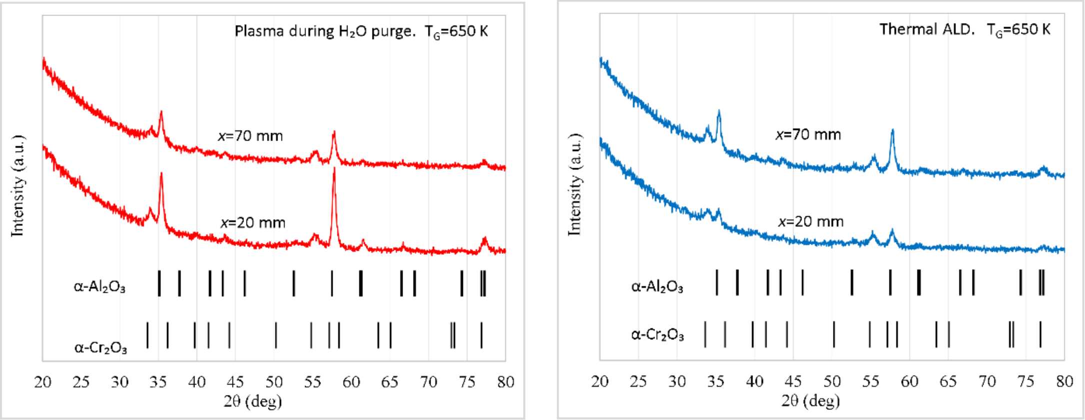

(**a**) (**b**)

**Figure 10.** GIXRD diffractograms of $Al_2O_3$ films deposited at a substrate temperature of 650 K on $\alpha$-$Cr_2O_3$ by (**a**) PEALD (plasma turned on during $H_2O$ purge) and (**b**) thermal ALD. During the deposition the samples were located at distances of 20 and 70 mm from the outlet of plasma tube.

Our previous study showed that compared with the purge following the TMA pulse, a markedly longer purge period was needed after the $H_2O$ pulse to obtain self-limited film growth [17]. Spectral measurements of the present study confirmed this result, as the OH band intensity decay after the $H_2O$ pulse was substantially slower than that of the Al lines observed after the TMA pulse (Figure 5). The likely reason for this is the gradual release of $H_2O$ to the gas phase from the surface due to the reaction between OH groups formed during the $H_2O$ pulse [38]:

$$\mathbf{2OH(ads.)} \rightarrow \mathbf{O(ads.)} + \mathbf{H_2O(gas)} \qquad (1)$$

and the subsequent formation of excited OH in the gas-phase reactions as explained in Section 3.1.3. As the surface hydroxyl groups are absorption sites for TMA [39], the decrease in the site concentration on the surface causes a reduction in GPC. Plasma applied during the $H_2O$ purge caused a significant (~ 10%) decrease in GPC compared with that obtained in thermal ALD (Table 1). However, the density of the film deposited by PEALD on the substrates located at a distance of 20 mm from the plasma tube were around 7% higher than the densities of other films (Table 1). Thus, the plasma applied during the $H_2O$ purge insignificantly influenced the mass growth per cycle (MGPC) at $x$ = 20 mm, while at $x$ = 70 mm, the effect of plasma on MGPC was considerable.

**Table 1.** Growth per cycle (GPC), density ($\rho$), mass growth per cycle ($MGPC = \rho \cdot GPC$) and surface roughness of films grown by thermal ALD and PEALD (plasma switched on during $H_2O$ purge) on substrates positioned at different distances from the plasma tube orifice. Films were deposited at 650 K on substrates coated with $\alpha$-$Cr_2O_3$.

| ALD Process | $x$, mm | GPC, nm | $\rho$, g/cm$^3$ | MGPC, ng/cm$^2$ | Roughness, nm |
|---|---|---|---|---|---|
| Thermal ALD | 20 | 0.104 ± 0.002 | 3.21 ± 0.06 | 33.4 ± 0.9 | 2.4 ± 0.1 |
| PEALD | 20 | 0.094 ± 0.002 | 3.43 ± 0.07 | 32 ± 1 | 3.3 ± 0.1 |
| Thermal ALD | 70 | 0.105 ± 0.002 | 3.27 ± 0.06 | 34.3 ± 0.9 | 1.5 ± 0.1 |
| PEALD | 70 | 0.092 ± 0.002 | 3.25 ± 0.06 | 29.9 ± 0.9 | 1.5 ± 0.1 |

A possible explanation for this difference is the plasma enhancement of the reaction described by Equation 1 on one hand and re-adsorption of OH radicals formed in plasma on the other hand. At

$x$ = 20 mm, the concentration of OH radicals in the gas phase was probably high enough to compensate the loss of surface OH groups while at $x$ = 70 mm, this kind of compensation was evidently not obtained. As the concentration of OH in the gas phase could not be very high even at $x$ = 20 mm, the re-adsorption was obviously a site-sensitive process supporting crystallization. With increasing $x$, the concentration of OH in the gas phase decreased (Figure 5) and, therefore, the contribution of OH re-adsorption to the crystal growth also decreased and became negligible.

The effect of possible plasma heating that could also promote the crystallization and influence GPC is not probable because the GPC values of the films deposited at higher gas temperature (inside plasma plume at $x = 20$ mm) and at lower gas temperature (at $x = 70$ mm) are the same while according to the results of our previous study, GPC should considerably decrease with increasing $T_G$. For example, $T_G$ increase from 620 to 650 K caused a GPC decrease from 0.115 to 0.089 nm [17]. In addition, the plasma turned on for the purge period following the TMA pulse did not cause changes in GPC.

A possible explanation for the fast decay of the plasma effect on the crystallization, observed with increasing $x$, was the corresponding decrease in the concentration of reactive species and short lifetime of those species. The formation of long-living $H_2O_2$ has also been observed in the plasma at atmospheric pressure in the presence of water vapor [40]. but under our conditions, the corresponding reaction is relatively slow (rate coefficient $k_1 \approx 4 \cdot 10^{-14}$ $cm^3s^{-1}$ at 400 K [41]) and the lifetime of OH seems to determine concentration profile of the reactive species in the gas phase. Although the quenching of the ground state OH radical, OH(X), is slower than that of the OH(A) state [42,43] , the convective transport of OH(X) from the OH-rich plasma plume region to the sample location at $x$ = 70 mm is still unlikely. For example, in the case of an Ar : 9% $H_2O$ mixture plasma at 200 Torr pressure, the OH density decay to 10% took up approximately 500 μs, whereas the OH diffusion losses were insignificant [44]. Considering 100 times lower pressure and linear velocity of gas in our reactor (1.1 m/s), such decay occurs already within 55 mm. Actually, this distance is expected to be even smaller as at our low pressure additionally OH diffusion losses should be significant. Spectral measurements that revealed a rapid decrease in the OH intensity and, consequently in the OH concentration with increasing $x$ (Figure 5c,d) confirmed this estimation.

## 4. Conclusions

The present study investigated the properties of low-pressure argon RF plasma, used in the plasma-enhanced atomic layer deposition of $Al_2O_3$ films. The plasma power, estimated from the recorded electrical characteristics was approximately 12 W. The argon metastable atom density in pure Ar plasma decreased10 times with increasing distance from the plasma tube orifice from 0 to 10 mm. The addition of ALD precursors reduced the density of metastable atoms down to the levels that were below the detection limit of the apparatus used. The gas temperature was estimated using the $N_2(C,v=2)$ rotational temperature, which was near the plasma tube orifice ≈400 K. Plasma spectra, measured during the TMA pulse, revealed TMA disintegration, as concluded from the appearance of Al lines and CN(B-X) bands. The $H_2O$ pulse caused a rapid increase in the OH(A-X,0-0) band intensity, indicating an effective OH production reaction between the Ar $1s_{2-5}$ atoms and $H_2O$ molecules.

It was proposed that the main plasma agents that helped $Al_2O_3$ crystallization were OH radicals. Plasma enhanced $Al_2O_3$ crystallization was observed only for samples located near the plasma tube orifice, inside the plasma plume where the OH concentration was high. Because of the rapid decay in OH concentration with distance, the plasma effect on crystallization was negligible at a distance of 70 mm from the tube orifice.

**Supplementary Materials:** The following supporting information can be downloaded: Figure S1: NH(A-X,0-0) band spectrum. Figure S2: Temperature estimation from Ar ($1s_5 \rightarrow 2p_6$) line shape analysis. Figure S3: TDLAS laser stability on the basis of Fabry-Pérot interferometer signal.

**Author Contributions:** Conceptualization, L.A. and J.A.; methodology, L.A., J.A and J.R; software, C.-T.P. and J.R.; validation, C.-T.P., J.R., L.A., I.J., R.T. and J.A.; formal analysis, C.-T.P., J.R., L.A., I.J., R.T. and J.A.; investigation, C.-T.P., J.R., and L.A; resources, L.A.; data curation, C.-T.P. and J.R.; writing—original draft

preparation, J.R.; writing—review and editing, C.-T.P., J.R., L.A., I.J., R.T. and J.A.; visualization, C.-T.P. J.R. and. L.A.; supervision, J.R. and L.A.; project administration, L.A.; funding acquisition, L.A. All authors have read and agreed to the published version of the manuscript.

**Funding:** This research was funded by Estonian Research Council grant PSG448.

**Data Availability Statement:** Data will be made available upon reasonable request.

**Acknowledgments:** The authors are thankful to Alma-Asta Kiisler and Aivar Tarre for technical assistance, and to Hugo Mändar for the access to X-ray analysis equipment and software.

**Conflicts of Interest:** The authors declare that they have no known competing financial interests or personal relationships that could have appeared to influence the work reported in this paper.

## References

1. Boris, D.R.; Wheeler, V.D.; Nepal, N.; Qadri, S.B.; Walton, S.G.; Eddy, C. (Chip) R. The Role of Plasma in Plasma-Enhanced Atomic Layer Deposition of Crystalline Films. *J. Vac. Sci. Technol. A Vacuum, Surfaces, Film.* **2020**, *38*, doi:10.1116/6.0000145.
2. Chang, J.; Chang, J.P. Achieving Atomistic Control in Materials Processing by Plasma-Surface Interactions. *J. Phys. D. Appl. Phys.* **2017**, *50*, doi:10.1088/1361-6463/aa71c7.
3. Faraz, T.; Arts, K.; Karwal, S.; Knoops, H.C.M.; Kessels, W.M.M. Energetic Ions during Plasma-Enhanced Atomic Layer Deposition and Their Role in Tailoring Material Properties. *Plasma Sources Sci. Technol.* **2019**, *28*, doi:10.1088/1361-6595/aaf2c7.
4. Faraz, T.; Knoops, H.C.M.; Verheijen, M.A.; Van Helvoirt, C.A.A.; Karwal, S.; Sharma, A.; Beladiya, V.; Szeghalmi, A.; Hausmann, D.M.; Henri, J.; et al. Tuning Material Properties of Oxides and Nitrides by Substrate Biasing during Plasma-Enhanced Atomic Layer Deposition on Planar and 3D Substrate Topographies. *ACS Appl. Mater. Interfaces* **2018**, *10*, 13158–13180, doi:10.1021/acsami.8b00183.
5. Profijt, H.B.; Kudlacek, P.; van de Sanden, M.C.M.; Kessels, W.M.M. Ion and Photon Surface Interaction during Remote Plasma ALD of Metal Oxides. *J. Electrochem. Soc.* **2011**, *158*, G88, doi:10.1149/1.3552663.
6. Knoops, H.C.M.; Faraz, T.; Arts, K.; Kessels, W.M.M. (Erwin) Status and Prospects of Plasma-Assisted Atomic Layer Deposition. *J. Vac. Sci. Technol. A Vacuum, Surfaces, Film.* **2019**, *37*, doi:10.1116/1.5088582.
7. Profijt, H.B.; Potts, S.E.; van de Sanden, M.C.M.; Kessels, W.M.M. Plasma-Assisted Atomic Layer Deposition: Basics, Opportunities, and Challenges. *J. Vac. Sci. Technol. A Vacuum, Surfaces, Film.* **2011**, *29*, doi:10.1116/1.3609974.
8. Wang, Z. Bin; Li, J.T.; Zhu, X.M.; Pu, Y.K. Determination of the de-Excitation Probability of Argon Metastable (1s5 and 1s3) Atoms on Aluminum, Stainless Steel, Silicon, Quartz and Pyrex Surfaces. *J. Phys. D. Appl. Phys.* **2015**, *48*, doi:10.1088/0022-3727/48/10/105203.
9. Wheeler, V.D.; Nepal, N.; Boris, D.R.; Qadri, S.B.; Nyakiti, L.O.; Lang, A.; Koehler, A.; Foster, G.; Walton, S.G.; Eddy, C.R.; et al. Phase Control of Crystalline Ga2O3 Films by Plasma-Enhanced Atomic Layer Deposition. *Chem. Mater.* **2020**, *32*, 1140–1152, doi:10.1021/acs.chemmater.9b03926.
10. Nepal, N.; Mahadik, N.A.; Nyakiti, L.O.; Qadri, S.B.; Mehl, M.J.; Hite, J.K.; Eddy, C.R. Epitaxial Growth of Cubic and Hexagonal InN Thin Films via Plasma-Assisted Atomic Layer Epitaxy. *Cryst. Growth Des.* **2013**, *13*, 1485–1490, doi:10.1021/cg3016172.
11. Fang, Z.; Williams, P.A.; Odedra, R.; Jeon, H.; Potter, R.J. Gadolinium Nitride Films Deposited Using a PEALD Based Process. *J. Cryst. Growth* **2012**, *338*, 111–117, doi:10.1016/j.jcrysgro.2011.10.049.
12. Fan, Q.; Sang, L.; Jiang, D.; Yang, L.; Zhang, H.; Chen, Q.; Liu, Z. Plasma Enhanced Atomic Layer Deposition of Cobalt Nitride with Cobalt Amidinate. *J. Vac. Sci. Technol. A Vacuum, Surfaces, Film.* **2019**, *37*, doi:10.1116/1.5062842.
13. Boris, D.R.; Wheeler, V.D.; Avila, J.R.; Qadri, S.B.; Eddy, C.R.; Walton, S.G. Role of Plasma Properties in Controlling Crystallinity and Phase in Oxide Films Grown by Plasma-Enhanced Atomic Layer Epitaxy. *J. Vac. Sci. Technol. A Vacuum, Surfaces, Film.* **2019**, *37*, doi:10.1116/1.5128208.
14. Raud, S.; Raud, J.; Aarik, L.; Jõgi, I.; Kivimäe, M.; Piller, C.T.; Plaas, M.; Plank, T.; Talviste, R.; Teesalu, T.; et al. The Production of Reactive Chlorine Species (RCS) by Argon and Helium Plasma Jets and the Sensitivity of Liver Cancer Cell HepG2 to RCS and H2O2 Treatment. *Plasma Process. Polym.* **2023**, 1–11, doi:10.1002/ppap.202300068.
15. Napari, M.; Tarvainen, O.; Kinnunen, S.; Arstila, K.; Julin, J.; Fjellvåg, S.; Weibye, K.; Nilsen, O.; Sajavaara, T. The $\alpha$ and $\gamma$ Plasma Modes in Plasma-Enhanced Atomic Layer Deposition with O2-N2 Capacitive Discharges. *J. Phys. D. Appl. Phys.* **2017**, *50*, doi:10.1088/1361-6463/aa59b3.
16. Catalin, C.; Dumitrache, C.; Bazavan, M.; Mitu, B.; Marascu, V.; Stancu, S.; Vizireanu, S.; Dinescu, G. Maximization of RONS Generation by Selection of Gas Nature and Injection Type in One-Electrode Tubular RF Cold Plasma Source. In Proceedings of the 2nd Annual Meeting of COST Action PlasTHER "Therapeutical applications of cold plasmas"; Bologna, 2023.

17. Aarik, L.; Piller, C.T.; Raud, J.; Talviste, R.; Jõgi, I.; Aarik, J. Atomic Layer Deposition of $\alpha$-Al2O3 from Trimethylaluminum and H2O: Effect of Process Parameters and Plasma Excitation on Structure Development. *J. Cryst. Growth* **2023**, *609*, 6–11, doi:10.1016/j.jcrysgro.2023.127148.
18. Aarik, L.; Mändar, H.; Tarre, A.; Piirsoo, H.M.; Aarik, J. Mechanical Properties of Crystalline and Amorphous Aluminum Oxide Thin Films Grown by Atomic Layer Deposition. *Surf. Coatings Technol.* **2022**, *438*, doi:10.1016/j.surfcoat.2022.128409.
19. Raud, J.; Jõgi, I.; Matisen, L.; Navratil, Z.; Talviste, R.; Trunec, D.; Aarik, J. Characterization of Ar / N 2 / H 2 Middle-Pressure RF Discharge and Application of the Afterglow Region for Nitridation of GaAs. *J. Phys. D. Appl. Phys.* **2017**, *50*, 505201.
20. Jõgi, I.; Raud, J.; Hein, K.; Laan, M. Spectral Characterization of Medium-Pressure RF Discharge in Argon-Oxygen Mixture. *J. Phys. D. Appl. Phys.* **2014**, *47*, doi:10.1088/0022-3727/47/33/335206.
21. Rezaei, F.; Gorbanev, Y.; Chys, M.; Nikiforov, A.; Van Hulle, S.W.H.; Cos, P.; Bogaerts, A.; De Geyter, N. Investigation of Plasma-Induced Chemistry in Organic Solutions for Enhanced Electrospun PLA Nanofibers. *Plasma Process. Polym.* **2018**, *15*, 1–18, doi:10.1002/ppap.201700226.
22. Thimsen, E.; Kortshagen, U.R.; Aydil, E.S. Nonthermal Plasma Synthesis of Metal Sulfide Nanocrystals from Metalorganic Vapor and Elemental Sulfur. *J. Phys. D. Appl. Phys.* **2015**, *48*, doi:10.1088/0022-3727/48/31/314004.
23. Kokai, F.; Yamamoto, K.; Koga, Y.; Fujiwara, S.; Heimann, R.B. Characterization of Ablation Plumes and Carbon Nitride Films Produced by Reactive Pulsed Laser Deposition in the Presence of a Magnetic Field. *Appl. Phys. A Mater. Sci. Process.* **1998**, *66*, 403–406, doi:10.1007/s003390050685.
24. Pearse, R.W.B.; Gaydon, A.G. *The Identification of Molecular Spectra*; second edi.; Chapman & Hall LTD.: London, 1950;
25. Morozov, A.; Krücken, R.; Ottenthal, T.; Ulrich, A.; Wieser, J. Ultraviolet Emission from Argon Water-Vapor Mixtures Excited with Low-Energy Electron Beams. *Appl. Phys. Lett.* **2005**, *86*, 3–5, doi:10.1063/1.1846155.
26. Tabayashi, K.; Shobatake, K. Dissociative Excitation of Water by Metastable Rare Gas Atoms: Rg( 3P0,2) +H2O→Rg+OH(A 2Σ+) +H (Rg=Ar,Kr). *J. Chem. Phys.* **1988**, *88*, 835–844, doi:10.1063/1.454163.
27. Mikhailov, D. V.; Pastor, A.A.; Serdobintsev, P.Y.; Timofeev, N.A.; Khodorkovskii, M.A. Discharge Plasma in an Argon–water Vapor Mixture as a Gas Laser Medium. *Russ. J. Phys. Chem. B* **2015**, *9*, 593–595, doi:10.1134/S1990793115040260.
28. Raud, J.; Laan, M.; Jgi, I. Rotational Temperatures of N<inf>2</inf>(C,0) and OH(A,0) as Gas Temperature Estimates in the Middle Pressure Ar/O<inf>2</inf> Discharge. *J. Phys. D. Appl. Phys.* **2011**, *44*, doi:10.1088/0022-3727/44/34/345201.
29. Nguyen, T.D.; Sadeghi, N. Rotational and Vibrational Distributions of N2(C) Excited by State-Selected Ar(3P2) and Ar(3P0) Metastable Atoms. *Chem. Phys.* **1983**, *79*, 41–55.
30. Raud, S.; Raud, J.; Jõgi, I.; Piller, C.T.; Plank, T.; Talviste, R.; Teesalu, T.; Vasar, E. The Production of Plasma Activated Water in Controlled Ambient Gases and Its Impact on Cancer Cell Viability. *Plasma Chem. Plasma Process.* **2021**, *41*, 1381–1395, doi:10.1007/s11090-021-10183-6.
31. Xiong, Q.; Nikiforov, A.Y.; Lu, X.P.; Leys, C. High-Speed Dispersed Photographing of an Open-Air Argon Plasma Plume by a Grating-ICCD Camera System. *J. Phys. D. Appl. Phys.* **2010**, *43*, doi:10.1088/0022-3727/43/41/415201.
32. Luque, J.; Crosley, D.R. LIFBASE: Database and Spectral Simulation Program (Version 1.5). *SRI Int. Rep.* **1999**, *9*.
33. Miura, N.; Hopwood, J. Spatially Resolved Argon Microplasma Diagnostics by Diode Laser Absorption. *J. Appl. Phys.* **2011**, *109*, 2458–2464, doi:10.1063/1.3531557.
34. Muñoz, J.; Dimitrijević, M.S.; Yubero, C.; Calzada, M.D. Using the van Der Waals Broadening of Spectral Atomic Lines to Measure the Gas Temperature of an Argon-Helium Microwave Plasma at Atmospheric Pressure. *Spectrochim. Acta - Part B At. Spectrosc.* **2009**, *64*, 167–172, doi:10.1016/j.sab.2008.11.006.
35. Raizer, Yuri, P. *Gas Discharge Physics*; Allen, J.E., Ed.; Springer-Verlag Berlin Heidelberg 1991, 1991; ISBN 3-540-19462-2Springer-Verlag Berlin Heidelberg New York.
36. Kramida, A., Ralchenko, Yu., Reader, J., and N.A.T. NIST Atomic Spectra Database (Ver. 5.10), [Online].
37. Zhu, X.M.; Pu, Y.K. A Simple Collisional-Radiative Model for Low-Temperature Argon Discharges with Pressure Ranging from 1 Pa to Atmospheric Pressure: Kinetics of Paschen 1s and 2p Levels. *J. Phys. D. Appl. Phys.* **2010**, *43*, doi:10.1088/0022-3727/43/1/015204.
38. Puurunen, R.L. Surface Chemistry of Atomic Layer Deposition: A Case Study for the Trimethylaluminum/water Process. *J. Appl. Phys.* **2005**, *97*, doi:10.1063/1.1940727.
39. Gosset, L.G.; Damlencourt, J.F.; Renault, O.; Rouchon, D.; Holliger, P.; Ermolieff, A.; Trimaille, I.; Ganem, J.J.; Martin, F.; Séméria, M.N. Interface and Material Characterization of Thin Al2O3 Layers Deposited by ALD Using TMA/H2O. *J. Non. Cryst. Solids* **2002**, *303*, 17–23, doi:10.1016/S0022-3093(02)00958-4.
40. Talviste, R.; Raud, S.; Jogi, I.; Plank, T.; Raud, J.; Teesalu, T. Investigation of a He Micro Plasma-Jet Utilized for Treatment of Prostate Cancer Cells. *Plasma Res. Express* **2019**, *1*, doi:10.1088/2516-1067/ab4ea9.

41. Atkinson, R.; Baulch, D.L.; Cox, R.A.; Hampson, R.F.; Kerr (Chairman), J.A.; Troe, J. Evaluated Kinetic and Photochemical Data for Atmospheric Chemistry: Supplement III. IUPAC Subcommittee on Gas Kinetic Data Evaluation for Atmospheric Chemistry. *J. Phys. Chem. Ref. Data* **1989**, *18*, doi:10.1063/1.555832.
42. Bruggeman, P.; Schram, D.; González, M.Á.; Rego, R.; Kong, M.G.; Leys, C. Characterization of a Direct Dc-Excited Discharge in Water by Optical Emission Spectroscopy. *Plasma Sources Sci. Technol.* **2009**, *18*, doi:10.1088/0963-0252/18/2/025017.
43. Del Greco, F.P.; Kaufman, F. Lifetime and Reactions of OH Radicals in Discharge-Flow Systems. *Discuss. Faraday Soc.* **1962**, *33*, 128–138, doi:10.1039/DF9623300128.
44. Tochikubo, F.; Uchida, S.; Watanabe, T. Study on Decay Characteristics of OH Radical Density in Pulsed Discharge in Ar/H2O. *Japanese J. Appl. Physics, Part 1 Regul. Pap. Short Notes Rev. Pap.* **2004**, *43*, 315–320, doi:10.1143/JJAP.43.315.